Extraction of Pre-earthquake Anomalies in Borehole Strain Data Using Graph WaveNet: A Case Study of the Lushan Earthquake

Chenyang Li [1], Yu Duan[1], Ying Han[2], Zining Yu[3], Chengquan Chi[1], * and Dewang Zhang[1], *

[1] School of Information Science and Technology, Hainan Normal University, Haikou, 571158, China
[2] College of Geography and Environmental Science, Hainan Normal University, Haikou, 571158, China
[3] Ocean University of China, College of information science and engineering, Qingdao, 266100, China

Correspondence to: Chengquan Chi (chicqhainnu@gmail.com), Dewang Zhang (zhangdwsan@163.com);

Abstract. On 20 April 2013, Lushan experienced a magnitude 7.0 earthquake. In seismic assessments, borehole strain meters, recognized for their remarkable sensitivity and inherent reliability in tracking crustal deformation, are extensively employed. However, traditional data processing methods encounter challenges when handling massive datasets. This study proposes using a graph wavenet graph neural network to analyze borehole strain data from multiple stations near the earthquake epicenter and establishes a node graph structure using data from four stations near the Lushan epicenter, covering years 2010–2013. After excluding the potential effects of pressure, temperature, and rainfall, we statistically analyzed the pre-earthquake anomalies. Focusing on the Guza, Xiaomiao, and Luzhou stations, which are the closest to the epicenter, the fitting results revealed two accelerations of anomalous accumulation before the earthquake. Approximately four months before the earthquake event, one acceleration suggests the pre-release of energy from a weak fault section. Conversely, the acceleration a few days before the earthquake indicated a strong fault section reaching an unstable state with accumulating strain. We tentatively infer that these two anomalous cumulative accelerations may be related to the preparation phase for a large earthquake. This study highlights the considerable potential of graph neural networks in con-ducting multi-station studies of pre-earthquake anomalies.

1 Introduction

Earthquakes result from the accumulation of stress in the Earth's crust during plate movement and collisions. Once the stress surpasses a critical threshold, the crust ruptures, unleashing seismic waves that reverberate through the ground, causing substantial dam-age (Campbell et al., 2020; Fan et al., 2021). Extensive research on earthquakes has generated a wealth of information worldwide, establishing a robust database for studying pre-earthquake anomalies.

On 20 April 2013, 08:02 UTC, a magnitude 7.0 earthquake struck Lushan County, Ya'an, Sichuan, China, within the Longmenshan fault zone. Researchers around the world have examined various phenomena preceding and following earthquakes, delving into subterranean, surface, and spatial changes. Chen et al., (2014) investigated the co-seismic ionospheric anomalies of the Lushan earthquake by employing a double-difference method that highlighted seismic-wave-induced acoustic wave propagation into the ionosphere. Guo and Zheng, (2022) proposed a big data-based method for

calculating and analyzing earthquake background noise and detecting anomalies within a 50-km radius of the epicenter 30-150 seconds before the Lushan earthquake. Liu et al., (2014b), discounting meteorological factors, analyzed aerosol optical depth (AOD) and observed elevated values four days prior, suggesting that AOD can be a potential earthquake precursor in the Sichuan Basin. Ground-water anomalies were examined by Liu et al., (2014a), who revealed medium-term dynamics and

35 short-term or imminent anomalies in water-level solid tide aberrations, emphasizing the importance of combining these anomalies to determine earthquake timing. Ma et al., (2015) analyzed pre-earthquake tidal cycles and concluded that celestial body tidal forces trigger earthquakes under critical rock fragmentation and sliding conditions. Zhang et al., (2016) explored thermal anomalies as earthquake precursors by processing and analyzing the sur-face temperature time series before the Lushan earthquake, and identified anomalies pre-dominantly near the Longmenshan fault zone. Zhu et al., (2013) analyzed

40 mobile gravity observations from 2010 to 2012, noting tectonic deformation and energy accumulation in the southern section of the Longmenshan fault zone, with implications for the relationship between the Wenchuan Ms8.0 and Lushan Ms7.0 earthquakes. Jiang et al., (2013) detected and analyzed vertical total electron content (VTEC) anomalies in the ionosphere, noting severe negative anomalies before and on the day of the earthquake, which correlated with the station distance relative to the epicenter.

45 Based on the findings from the United States Plate Boundary Observation (PBO) project proposal, borehole strain observations have emerged as superior to GPS and laser strain meters in capturing short- to medium-term, as well as pro-earthquake, strain variations (Zhang, 2004; Zheng and Zhang, 2004). China has deployed multiple four-component borehole strainmeters, offering not only four-component data but also auxiliary observations of air pressure, groundwater level, and temperature (Chi et al., 2007; Qiu, 2014; Qiu et al., 2020). Numerous studies on the Lushan earthquake have employed

50 borehole strain data. Qiu et al., (2013) correlated borehole strain data from the Guza station before the Lushan Ms7.0 earthquake with other influencing factors, establishing a connection to the earthquake. Zhu et al., (2018) identified the precursors of the Lushan earthquake by analyzing the eigenvalues and eigenvectors from borehole data. Yu et al., (2021) employed a state-space model to decompose the strain into component responses and discovered the synchronous acceleration of approximate negative entropy anomalies at multiple stations four to six months before an earthquake. Liu et

55 al., (2019) used the S-transform method to analyze the time-frequency characteristics of borehole strain data, revealing reliable anomalies that reflect the entire process of pre-earthquake, during, and post-earthquake strain changes. Chi, (2013) uncovered a "tidal aberration" phenome-non, persisting over three months before the earthquake, with significant strain changes occurring 15 to 19 days prior. Tang and Jing, (2013) conducted an analysis of surface strain co-seismic orders, noting differences between the Wenchuan and Lushan earthquakes related to earthquake magnitude. Despite the valuable insights gained from these studies, they mostly focused on single-station data, overlooking the potential correlations between

60 multiple stations.

As earthquake monitoring data accumulates, traditional processing methods face challenges in managing vast quantities of data. The emergence of deep learning, particularly graph neural networks (GNNs), has markedly enhanced prediction and classification accuracy, particularly for non-Euclidean spatial data characterization (Kipf and Welling, 2016; Niepert et al.,

65   2016; Scarselli et al., 2009; Wu et al., 2019; Zhou et al., 2020). Recent developments in spatiotemporal GNN frameworks integrate GNNs with various event-learning methods to extract complex dependencies (Oord et al., 2016; Rathore et al., 2021; Yu et al., 2017). Kim et al., (2022) utilized raw waveform data from multiple stations to classify earthquake events, demonstrating the effectiveness of GNNs in aggregating features from individual stations. Bilal et al., (2022) refined earthquake magnitude, depth, and location predictions by extracting features from waveform data from multiple stations and

70   integrating earthquake catalog information in-to a GNN. Huang et al., (2023) applied a Graph Attention Isomorphic Network (GAIN) to analyze earthquake catalogs and geomagnetic signals, successfully detecting pre-earthquake anomalies. These studies highlighted the significant potential of GNNs in earthquake research.

In this study, we proposed an innovative method for extracting pre-earthquake anomalies from borehole strain data using Graph WaveNet. To analyze borehole strain data from multiple stations for the Lushan earthquake, our study employed the

75   flowchart shown in Fig. 1.
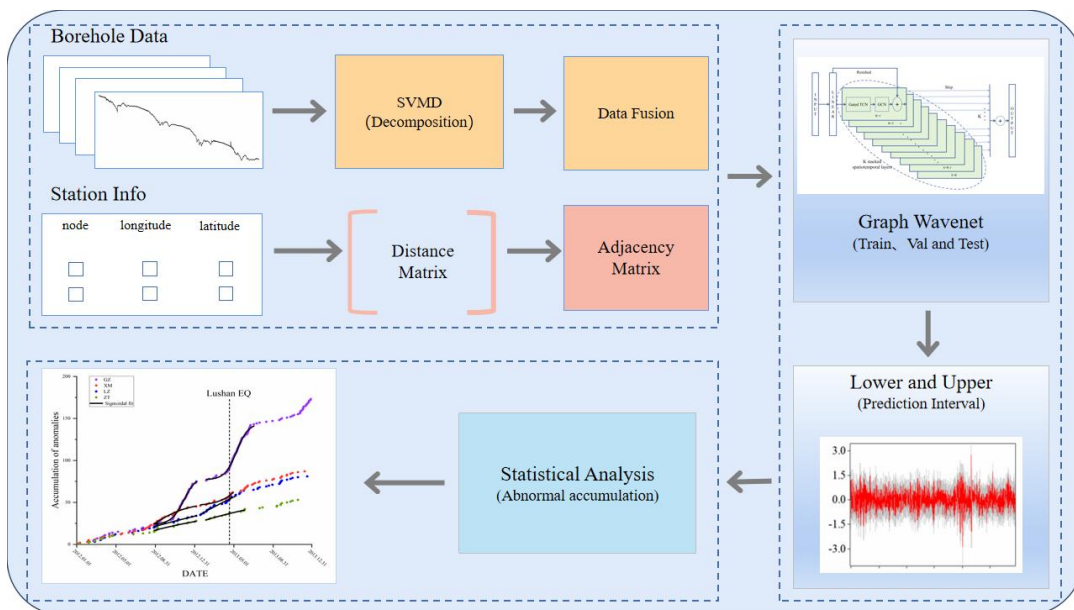
Figure 1: The framework of borehole strain data processing and pre-earthquake anomaly detection.

As shown in Fig. 1, the process begins with the conversion of data from the four-component borehole into strain. Subsequently, the borehole data are decomposed using the segmented variational modal method (SVMD), and the resulting

80   decomposed outcomes were fused. By calculating distances between stations using longitudinal and latitudinal coordinates, a distance matrix is constructed and then normalized to form an adjacency matrix. The fused data and adjacency matrix serve as inputs for training, vali-dation, and prediction using the graph wavenet GNN. During the prediction phase, upper and lower bound prediction intervals are established based on the model's output. Anomalies were identified by comparing the prediction intervals with the original data. The cumulative values of pre-earthquake anomalies in the borehole strain data

85   from various stations were subsequently subjected to statistical analyses.

The remained of this article is structured as follows: the two sections delve into the specifics of the Lushan earthquake, providing an introductory exploration of the event and the borehole data pivotal to our analysis. In the third section, we introduce the SVMD and delve into the theoretical underpinnings of the graph wavenet network, laying the groundwork for a comprehensive understanding of our analytical approach. A detailed case study of the Lushan earthquake follows, providing
90 a tangible illustration that guides readers through the intricacies of our data-processing methodology. Section five unveils the anticipated results, predicted outcomes, and cumulative anomaly values. Furthermore, it outlines the application of statistical methods for identifying pre-earthquake anomalies related to the Lushan earthquake. The final section presents the conclusions of the study and summarizes the key insights drawn from our analysis.

2 Observation Data and Earthquakes

95 A formidable 7.0 magnitude earthquake struck Lushan County, Ya'an, Sichuan Province, at 8:02 am on 20 April 2013. The epicenter was located at approximately 103° E and 30.30° N within the Longmenshan Fault Zone at a depth of 13 km. The earthquake mechanism solution revealed a retrograde rupture of the earthquake-induced rupture. By 24 April 2013, the earthquake had triggered over 4,000 aftershocks, affecting more than 300,000 people across an expansive area exceeding 12,000 km². The aftermath witnessed a significant loss of life and property. Additionally, the seismic event triggered various
100 geo-logical hazards, such as earth fissures, landslides, and surface deformation (Hong et al., 2013).
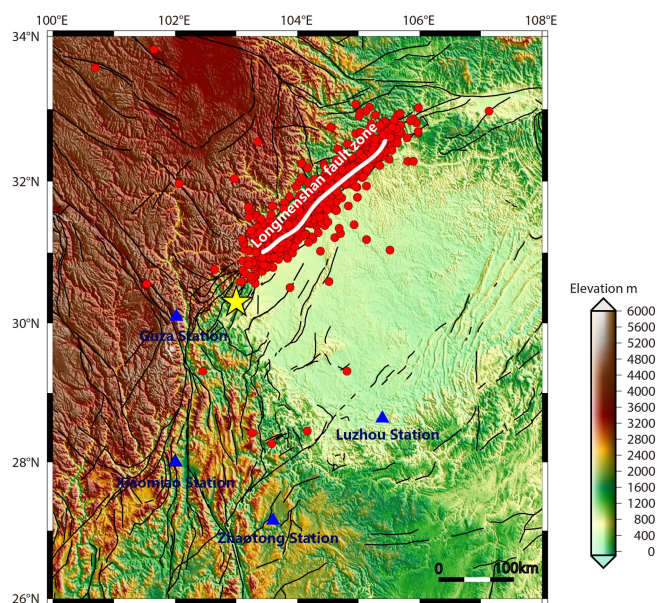
Figure 2: Location of the four observation stations relative to the epicenter of the Lushan earthquake. The blue triangles represent the locations of the borehole strain observation stations. The yellow star represents the epicenter of the Lushan earthquake, while the white curve depicts the Longmenshan fault zone. This map was generated by GMT software, v. 6.0.0rc5 (https://gmt-
105 **china.org/).**

Dobrovolsky's estimate of the radius of influence of precursors for earthquakes of different magnitudes is shown in the following Eq. (1) (Dobrovolsky et al., 1979):

$$\rho = 10^{0.43M} \text{ km},\tag{1}$$

where M denotes the magnitude and ρ denotes the radius of influence of M magnitude. The Lushan 7.0 magnitude earthquake's radius of influence extends approximately 1023 km. Among the selected monitoring stations, Guza is situated 73 km from the epicenter, while Xiaomiao, Luzhou, and Zhaotong are positioned at distances of 268 km, 286 km, and 337 km from the epicenter, respectively. This positioning confirms that the chosen stations possess the capability to monitor earthquake-related anomalies. Detailed information about Guza, Xiaomiao, Luzhou, and Zhaotong, including latitude and longitude coordinates, distance from the Lushan earthquake's epicenter, rock type at the drill borehole locations, and borehole depth, is provided in Table 1. Figure 2 visually depicts the geographical locations of the four observation stations relative to the epicenter of the Lushan earthquake.

Table 1. Information on borehole strain stations was used in this study.

Station Name	Locations	Rock Type	Borehole Depth(m)	Epicentre Distance(km)
GuZa	30.12° N,102.18° E	Granite	40.69	73
XiaoMiao	28.00° N, 102.00° E	Siltstone	41.78	268
LuZhou	28.87° N, 105.42° E	Quartz Sandstone	40	286
ZhaoTong	27.32° N, 103.73° E	Basalt	45	337

The four-component borehole strainmeter serves to observe the temporal inverse of displacement at a specific point, offering insights not attainable through GPS and seismometers. Operating with a continuous recording frequency of one sample per minute, it significantly enhances temporal resolution by at least one order of magnitude. Additionally, its observation bandwidth surpasses that of seismometers, particularly at the long-period end of the spectrum. This specialized strainmeter comprises four horizontally positioned sensors designed to measure changes in borehole diameter. These sensors are strategically spaced at a 45° angle, and the relationship between the four measurements from the strainmeter can be expressed as follows (Qiu et al., 2009; Su, 2019):

$$S_1 + S_3 = k(S_2 + S_4),\tag{2}$$

This Eq. (2) represents the self-consistent formulation for a four-component borehole strain strainmeter. The self-consistent coefficient, denoted as k, ideally equals 1, and data is deemed reliable when k is greater than or equal to 0.95. Strain conversion is achieved through the following Eq. (3) using the four measurements:

$$\begin{cases} S_{13} = S_1 - S_3 \\ S_{24} = S_2 - S_4 \\ S_a = (S_1 + S_2 + S_3 + S_4)/2 \end{cases},\tag{3}$$

In this Eq. (3), S_{13} and S_{24} represent two independent shear strains. Shear strain pertains to alterations in the total area or volume of an object while maintaining a deformed shape. Additionally, S_a denotes surface strain, signifying changes in area without a concurrent shift in the object's morphology. This characteristic is observed in the presence of hydrostatic enclosure

pressure (Su, 2019). For the analysis in this paper, S_a data from four stations—Guza, Xiaomiao, Luzhou, and Zhaotong— were specifically selected for examination.

3 Methods

3.1 Segmented Variational Modal Decomposition

A Borehole Strain Signal, characterized as a typical nonstationary signal, can be effectively analyzed by decomposing it into a set of Intrinsic Mode Functions (IMFs) using the Empirical Mode Decomposition (EMD) method. However, EMD encounters challenges such as mode aliasing. To address this issue, an adaptive time-frequency analysis algorithm, the Variational Mode Decomposition (VMD), was introduced by Dragomiretskiy and Zosso, (2014). The VMD exhibits superior noise immunity in signal processing, providing an effective solution to these challenges. This approach has been successfully applied by Huang et al., (2022) and Zhang and He, (2023) to process raw earthquake waveforms, yielding improved decomposition results.

VMD stands as a non-recursive signal processing method designed to decompose a time series into a sequence of intrinsic mode functions characterized by limited band-width. The decomposition process essentially involves solving variational problems, and the variational model can be expressed as follows:

$$\begin{matrix} min \\ \{u_k\},\{\omega_k\} \end{matrix} \sum_{k=1}^{K} \left\| \partial_t \left\{ \left[\left(\delta(t) + \frac{j}{\pi t}\right) * u_k(t) \right] e^{-j\omega_k t} \right\} \right\|_2^2$$

$$s.t. \sum_{k=1}^{K} u_k(t) = f(t) , \tag{4}$$

where $\{u_k\} = \{u_1, u_2, ..., u_K\}$、$\{\omega_k\} = \{\omega_1, \omega_2, ..., \omega_K\}$ are the k modal functions and the corresponding center frequencies of the signal decomposition, respectively; ∂_t is the bias computation for time t; $\delta(t)$ is the unit impulse function; j is the imaginary unit; $*$ is the convolution computation.

To solve the variational model, a quadratic penalty term α and the Lagrange multiplier operator $\lambda(t)$ are introduced to make the variational model unconstrained. The constructed generalized Lagrangian function is:

$$L(\{u_k\}, \{\omega_k\}, \lambda) = \alpha \sum_{k=1}^{K} \left\| \partial_t \{ [(\delta(t) + \frac{j}{\pi t}) * u_k(t)] e^{-j\omega_k t} \} \right\|_2^2$$

$$+ \left\| f(t) - \sum_{k=1}^{K} u_k(t) \right\|_2^2 + \langle \lambda(t), f(t) - \sum_{k=1}^{K} u_k(t) \rangle , \tag{5}$$

where L denotes the Lagrangian generalization operator; α denotes the data fidelity constraint function; λ denotes the Lagrangian multiplier.

The alternating direction multiplier method (ADMM) is used to solve Eq. (5), and the iterative optimization of u_k, ω_k, and λ. The iterative formulas for the mode u_k, the corresponding center frequency ω_k, and the Lagrange multiplier λ can be updated as:

$$\hat{u}_k^{n+1}(\omega) = \frac{\hat{f}(\omega) - \sum_{i \neq k} \hat{u}_i(\omega) + \frac{\hat{\lambda}(\omega)}{2}}{1 + 2\alpha(\omega - \omega_k)^2}$$

$$\omega_k^{n+1} = \frac{\int_0^\infty \omega |\hat{u}_k(\omega)|^2 dw}{\int_0^\infty |\hat{u}_k(\omega)|^2 dw}$$

$$\hat{\lambda}^{n+1}(\omega) = \hat{\lambda}^n(\omega) + \tau(\hat{f}(\omega) - \sum_k \hat{u}_k^{n+1}(\omega)), \qquad (6)$$

where $\hat{u}_k^{n+1}$ is the kth IMF component in the n+1st iteration; ω_k^{n+1} is the center frequency corresponding to $\hat{u}_k^{n+1}$; $\hat{\lambda}^{n+1}(\omega)$ is the value of the Lagrangian operator in the n+1st iteration, and τ is the noise tolerance of the signal. Set the termination condition of the algorithm as:

$$\sum_{k=1}^K \frac{\left\| \hat{u}_k^{n+1} - \hat{u}_k^n \right\|_2^2}{\left\| \hat{u}_k^n \right\|_2^2} < \varepsilon, \qquad (7)$$

where ε denotes the discrimination accuracy.

In this study, we employ a method of applying Variational Mode Decomposition (VMD) to data segments through the incorporation of sliding windows (SVMD). This approach effectively addresses the challenge of limited memory when conducting VMD on the entire dataset while retaining the correlation between the data points (Chi et al., 2023). The fundamental principle of the SVMD method is illustrated in Fig. 3.
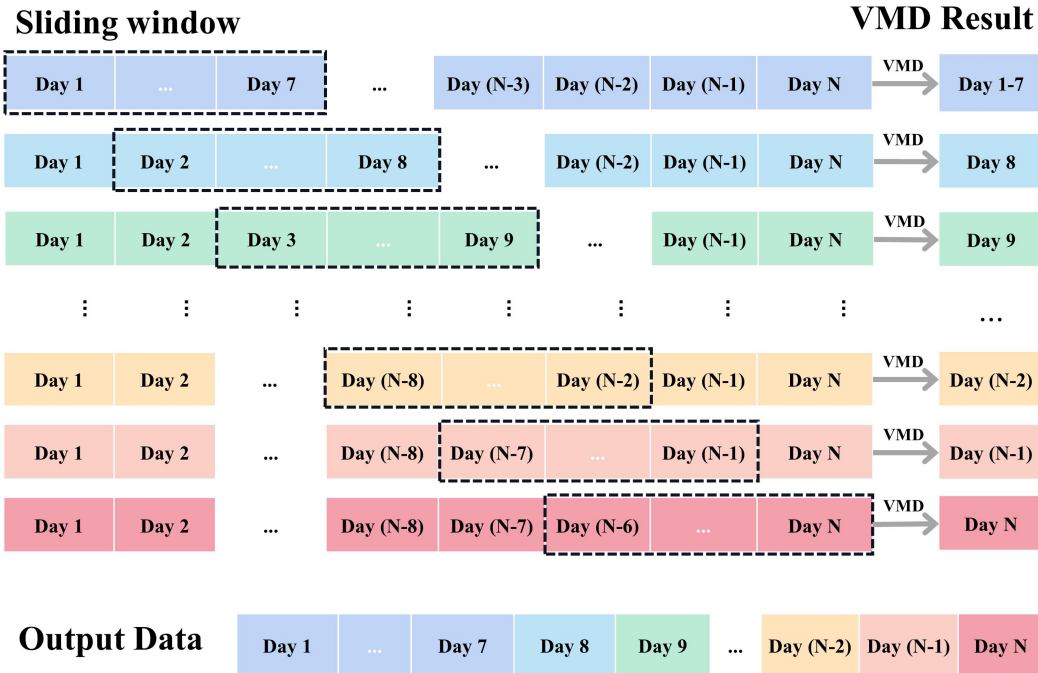
Figure 3: Schematic diagram of Segmented Variational Modal Method (SVMD) principle.

As depicted in Fig. 3, we opt for a consistent sliding window approach with a size of 7 days and a sliding step of 1. The initial sliding window encompasses all the data from the first 7 days. From the second sliding window onwards, only the data from the last day of the current window is preserved and concatenated behind the results obtained from the previous window.

3.2 Graph Wavenet Neural Network Architecture

3.2.1 Gated Temporal Convolutional Network for Extracting Temporal Features

180 During the processing of the time-series data, Causal Convolution maintains the causal relationships inherent within the data. This technique facilitates the extraction of time-series features through convolution. However, as the sequence length increases, capturing temporal dependence requires more convolution layers, thereby substantially increasing computational demands. To address this challenge, an expansion factor was introduced for Causal Convolution. The inclusion of this expansion factor can enlarge the receptive field of the Causal Convolution, enabling the capture of longer time-series

185 features with a reduced number of convolutional layers. The relationship between the input sequence length L_{in} after causal dilation convolution and the output sequence length L_{out} can be expressed as:

$$L_{out} = L_{in} + padding - (d \times (k - 1)) , \qquad (8)$$

where L_{out} is the length of the output sequence; L_{in} is the length of the input sequence; padding is the number of zero paddings added to the ends of the input sequence, which are added at the beginning of the sequence to preserve causality; k

190 is the size of the convolution kernel, which is a small, learnable weight matrix; and d is the dilation factor, which indicates the span of the convolution kernel over the input sequence, with larger dilation factors being able to capture long-term time dependencies. The dilation causal convolution with a convolution kernel size of 2 and a sliding step of 1 is shown in Fig. 4a.
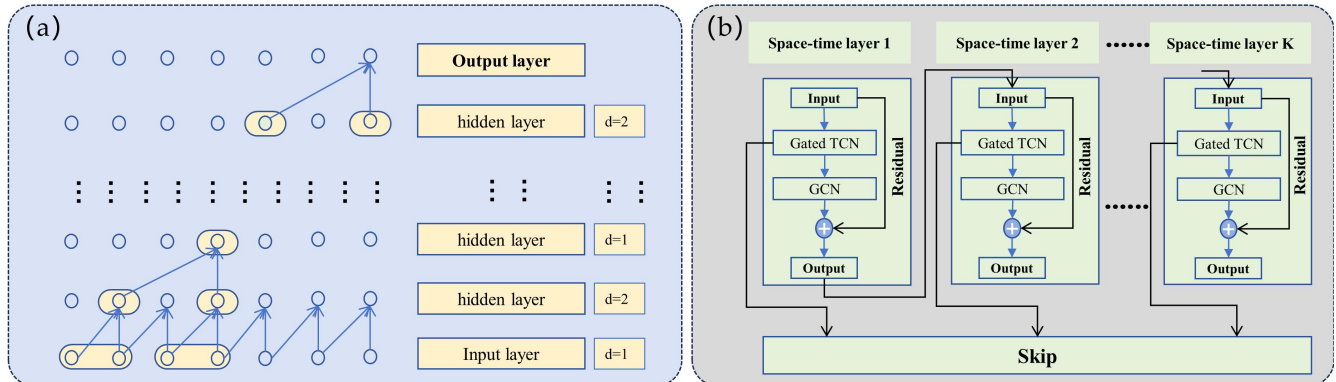
Figure 4: (a) Schematic of Dilated Causal Convolutional Layers. (b) Temporal-Spatial Layers architecture.

195 Although Convolutional Neural Networks (CNNs) are commonly employed for image processing, 1D CNNs can also be effectively used for time-series analysis. Gated Temporal Convolutional Networks (TCN) leverage 1D CNNs to extract features from time-series data. This architecture comprises two key modules: one for convolving the input to extract features by employing tanh as the activation function, and the other for controlling the amount of information passed from the current layer to the next layer by utilizing the sigmoid activation function. The Gated TCN module is defined as:

200 $$T = \tanh(W_1 * x + b_1) \bullet \text{sigmod}(W_2 * x + b_2) , \qquad (9)$$

where W_1 and W_2 represent the weight parameters, b_1 and b_2 represent the corresponding bias parameters, and $\bullet$ denotes convolution.

3.2.2 Graph Convolutional Networks for Extracting Spatial Features

The fundamental concept of a graph network is to represent interactions among real features based on spatial dependence
205 dictated by the graph structure. The distance adjacency matrix is symmetrically normalized to function as an adjacency
matrix for graph convolution. This approach effectively captures the node information and preserves the graph structure. By
constructing an undirected complete graph for each station, where all nodes are directly connected, each node interacts solely
with its neighboring nodes for information exchange. To ensure that input features encompassed all information in the
current node and its first-order nearest neighbor nodes, a first-order symmetric normalized adjacency matrix was selected
210 during the graph convolution process. The convolution layer of the graph is defined as:

$$H^{(l+1)} = \sigma(\widetilde{D}^{-\frac{1}{2}} \cdot \widetilde{A} \cdot \widetilde{D}^{-\frac{1}{2}} \cdot H^{(l)} \cdot W^{(l)}) \,, \tag{10}$$

where $H^{(l)}$ denotes the embedding vector of layer l; $H^{(l+1)}$ denotes the embedding vector of layer $(l+1)$; $\widetilde{D}^{-\frac{1}{2}} \cdot \widetilde{A} \cdot \widetilde{D}^{-\frac{1}{2}}$
denotes the symmetric normalized adjacency matrix of the current layer; where D denotes the degree matrix and $\widetilde{A}$ denotes
the Distance Adjacency Matrix; $W^{(l)}$ denotes the weight of the neural network in the current convolutional layer; and σ
215 denotes the nonlinear activation function of the neural network. Introducing a dropout rate to the output of each training
batch in graph convolution involves randomly ignoring half of the hidden layer nodes.

This dropout strategy was applied across different neural networks, and "opposite" fits were averaged. This aids in
mitigating overfitting because conflicting tendencies can cancel each other out during the training process.

3.2.3 Temporal-Spatial Layers

220 Figure 4b illustrates the structure of the spatiotemporal layer. Each layer within the spatiotemporal layer captures temporal
dependencies using Gated TCNs. This involved utilizing node features produced by the TCN module and the graph's
adjacency matrix as inputs for the Graph Convolutional Network (GCN) module. The GCN layer is responsible for capturing
spatial-temporal features, and the spatial-temporal features of the current layer are residual and linked to the input, serving as
inputs to the subsequent spatial-temporal layer. The output of the Gated TCN module serves as the output of the current
225 spatial-temporal layer, and the outputs of all spatial-temporal layers are interconnected using skip connections. This design
facilitated the capture of short-term and spatial dependencies.

3.2.4 Graph Wavenet Neural Network Framework

Figure 5 illustrates the framework of a graph wavenet. The initial step involved pre-processing the multistation borehole data
and converting the latitude and longitude of each station into an adjacency matrix. Subsequently, the data underwent a
230 dimensionality increase in the linear layer, followed by processing in the Gated TCN module to obtain the current
information. The output of the Gated TCN module is then employed to extract spatial information through the GCN layer.
The extracted spatial and temporal information is connected to the input of the current layer, which serves as the input for the
subsequent spatial and temporal layers, which can capture both the current and historical information using different dilation

factor sizes. Finally, the information extracted from each Gated TCN layer is aggregated into an output layer. The output
235 sequence was downscaled using the ReLU activation function and a linear layer. The upper and lower bounds of the output
sequence were calculated using the normal distribution method. The prediction intervals of the network were constructed
from the upper and lower bounds. The upper and lower bounds of the prediction intervals are determined using the following
formulas:

$$Lower = Prediction + Z \times \text{std\_error}$$

240 $$Upper = Prediction - Z \times \text{std\_error} \, , \tag{11}$$

where $Prediction$ is the predicted value; Z is the Z-Score of the normal distribution, which is about 1.96 for a 95%
confidence level; and std_error is the root mean square error.
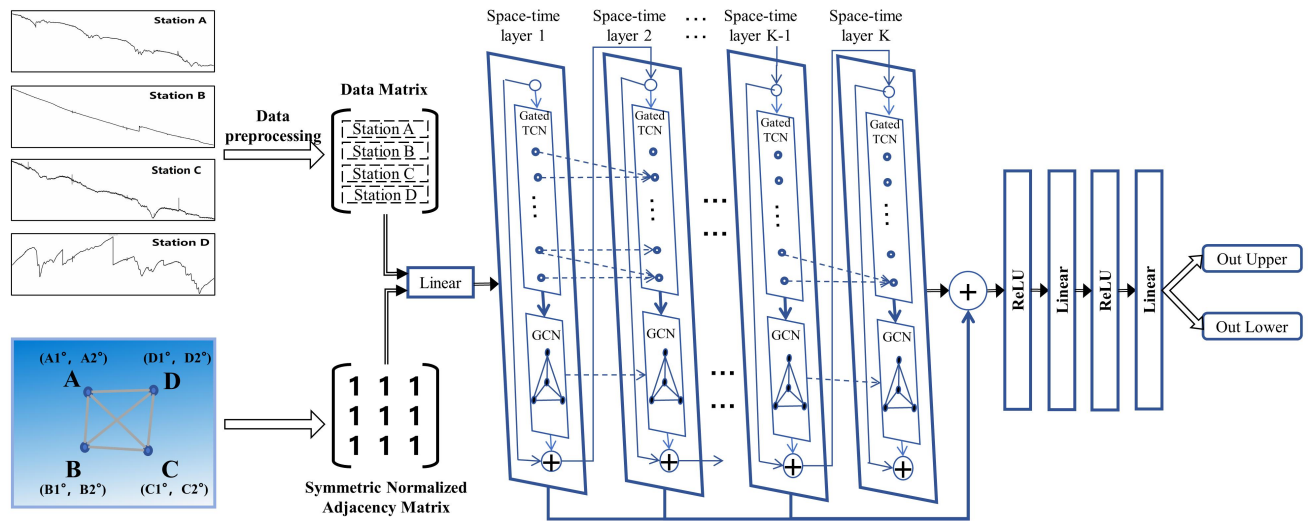
Figure 5: Framework of Graph Wavenet.

245   For the graph wavenet neural network model, Mean Absolute Error (MAE) was employed as the loss function for
backpropagation during training. A dropout of 0.3 was ap-plied during graph convolution to enhance the model's
generalization. The Adam optimizer was utilized to update the weights, with a learning rate of 0.001 and a weight decay rate
of 0.0001. This configuration allowed the model to decay, effectively preventing over-fitting by reducing parameter
magnitudes. The number of training rounds for the model was set to 100.

250 **4 Data Processing**

We analyzed the four-component borehole strain data collected from Guza, Xiaomiao, Luzhou, and Zhaotong stations from
1 January 2010 to 31 December 2013. Initially, the data from each station were validated using self-consistent equations.
Subsequently, the four-component borehole strain data from each station were transformed into two shear strains, S_{13} and

S_{24}, and one surface strain, S_a, using a strain conversion equation. Figure 6a shows the data series of surface strain S_a after

255   converting the borehole strain data from each of the four stations.
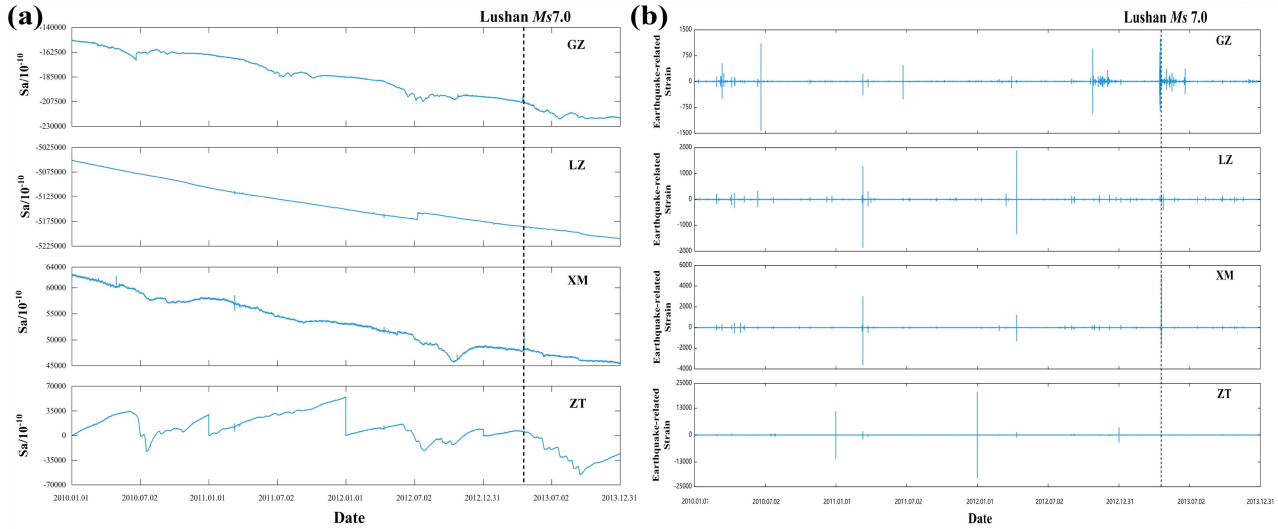
Figure 6: (a) S_a of the borehole strain data from 2010 to 2013 for the Guza, Xiaomiao, Luzhou, and Zhaotong stations. **(b)** SVMD results of S_a components for Guza, Xiaomiao, Luzhou and Zhaotong stations.

Subsequently, the S_a data from each of the four stations were decomposed using the Segmented Variational Modal

260   Method (SVMD). The decomposition parameters were set to a bandwidth of 2,000, the number of modes decomposed to five, and the convergence accuracy to 10^{-7}. The results of the SVMD decomposition were compared with data related to the influencing factors, effectively eliminating the effects of seasonal trends and solid tides. The extracted modes are specifically related to crustal activity, showcasing short-period, high-frequency oscillatory signals associated with earthquake variations in earthquake strain within crustal motions (Chi et al., 2019). The time-series data after SVMD decomposition of S_a data

265   from each station are illustrated in Fig. 6b.

The next step involved data fusion, with SVMD applied to the S_a component data from different stations to extract data related to crustal activities. The construction of the GNN required information from each node; hence, the information from multiple stations was fused as inputs to the GNN, and the data matrix R_a of the constructed R_a component is shown below:

$$R_a = \begin{bmatrix} GZ_a(t_1) & GZ_a(t_2) & ... & GZ_a(t_{2103840}) \\ LZ_a(t_1) & LZ_a(t_2) & ... & LZ_a(t_{2103840}) \\ XM_a(t_1) & XM_a(t_2) & ... & XM_a(t_{2103840}) \\ ZT_a(t_1) & ZT_a(t_2) & ... & ZT_a(t_{2103840}) \end{bmatrix}^T,$$ (12)

270   Where GZ , LZ , XM , and ZT represent the Guza, Luzhou, Xiaomiao, and Zhaotong stations, respectively; a indicates the selection of the surface strain S_a component data; t denotes the length of the time series; and T denotes the transpose; and the fused data matrix R serves as the input for the node information in the Graph Wavenet GNN. The constructed data matrix has a minute sampling interval with 1,440 data sampling points per day. The data matrix undergoes processing using a sliding window with a length of 60, where the sliding window size of 60 corresponds to one hour. A sliding window was

275 implemented to predict the next hour's data based on the current hour's data. The sampled data are considered as the features of the sample, and the data shape is constructed as a tensor of [64, 60, 4, 1], where 64 denotes the sample length and [60, 4, 1] represents the input or output of a single data point. In this context, 60 signifies the sequence length, 4 is the number of nodes, and 1 is the number of node features. The selected data spanned 2010 to 2013, divided chronologically in a ratio of 3:1:4. Specifically, 2010 and 2011 were allocated as the training and validation sets, respectively, whereas 2012 and 2013

280 were used as the test set.

The subsequent step involved constructing the adjacency matrix of the graph. A node graph of the four stations is shown in Fig. 7. The graph is defined as $G = (V, E)$, where V corresponds to the set of nodes and E corresponds to the set of edges in the graph. The relationship between edges and nodes is expressed as $E_{ij} = (V_i, V_j)$, $V_i, V_j \in V$. Graphs are commonly represented using an adjacency matrix, where the adjacency matrix A is a $N \times N$ square and N denotes the number of nodes.

285 The graph is written as $Aij = 1$ if two vertices, i and j, are connected by an edge and 0 otherwise. The number of neighboring nodes for node V is referred to as the degree of that node, and the degree matrix D is an $N \times N$ diagonal array, with the elements on the diagonal being the degrees of individual vertices: $D(V_i) = N(i)$.
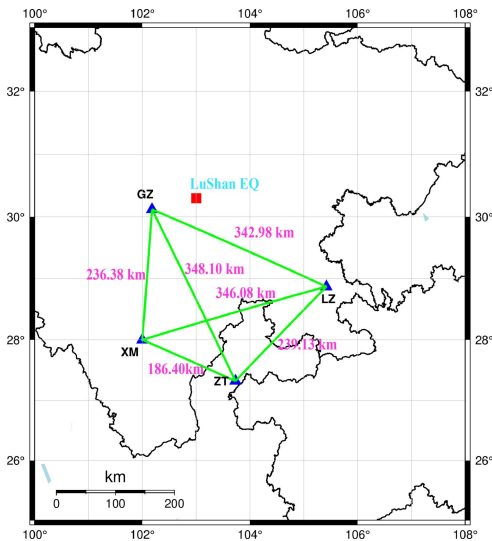
Figure 7: Node diagram of the four borehole strain observation stations constructed. The blue triangles indicate the locations of
290 the four borehole strain stations, the green line indicates the distance between the two stations, and the red square indicates the
epicenter of the Lushan earthquake.

The true distance between the stations was calculated using the corresponding latitude and longitude data of any two stations. Assuming that the Earth is a standard sphere, the principle for calculating the distance in latitude and longitude coordinates involves determining the distance between two points on the sphere, equivalent to the arc length of a cross-

295 sectional circle. For any two given points and their corresponding latitudes and longitudes, $A(N1, E1)$ and $B(N2, E2)$, with the average radius of the Earth as R and the center of the Earth as the midpoint of the right angle coordinates, A and B represent two points corresponding to the right angle coordinates:

$A(R\cos(N1)\cos(E1)), R\cos(N1)\sin(E1), R\sin(N1))$,$A(x_1, y_1, z_1)$

$B(R\cos(N2)\cos(E2)), R\cos(N2)\sin(E2), R\sin(N2))$,$B(x_2, y_2, z_2)$, (13)

300 We calculated the angle between two points based on the coordinates of points A and B. Let the angle between A and B be α; then, the cosine of the angle $\cos\alpha$ is calculated as follows:

$$\cos\alpha = \frac{x_1*x_2 + y_1*y_2 + z_1*z_2}{\sqrt{(x_1^2+y_1^2+z_1^2)} * \sqrt{(x_2^2+y_2^2+z_2^2)}},$$ (14)

Thus, the distance d between two points can be expressed as:

$$d = R*arccos(cos\alpha),$$ (15)

305 The distance between two stations was determined by calculating the latitude and longitude coordinates of any two stations. Subsequently, an adjacency distance matrix for the node graph is constructed based on these distances. To optimize the adjacency matrix for use in the Graph Wavenet GNN, the distances between the nodes were normalized to represent the weights between them. This normalized adjacency matrix was then utilized in the Graph Wavenet model.

5 Results
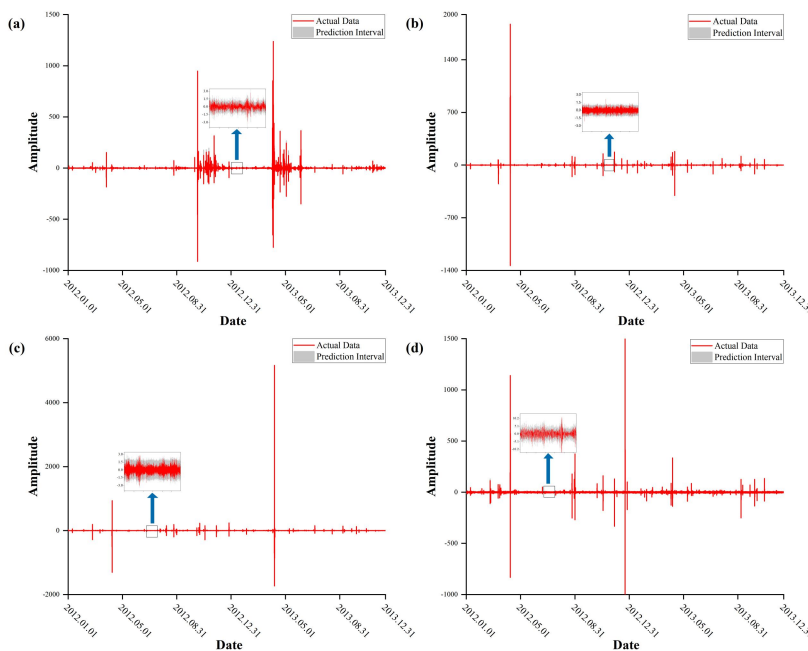
310

Figure 8: Graph WaveNet graph neural network prediction results; red lines indicate real data and gray areas indicate prediction intervals. (a) Results of the Lushan earthquake prediction from Guza station; (b) Results of the Lushan earthquake prediction from Luzhou station; (c) Results of the Lushan earthquake prediction from Xiaomiao station; (d) Results of the Lushan earthquake prediction from Zhaotong station.

315 In this study, we employed a Graph Wavenet GNN to analyze borehole data from multiple stations prior to the Lushan earthquake. The analysis focused on extracting pre-earthquake anomalies based on the results obtained. Anomalies were identified when the raw data surpassed the corresponding upper or lower prediction intervals established by the network. The prediction results for each station are shown in Fig. 8.

As shown in Fig. 8, our raw data closely align with the predicted intervals, demonstrating the Graph Wavenet accurate
320 prediction of borehole data at each station. To identify point anomalies in the borehole strain data predictions, we employed the following criteria: (a) detecting more than 15 points outside the intervals within a 30-minute window; (b) identifying difference between the center of predicted intervals and the actual values exceeding 1.5 times the bandwidth of the intervals, with more than three such points in the same 30-minute period. Days meeting these conditions were considered anomalous (Chi et al., 2023). To validate whether the extracted anomalous days were earth-quake-related, we randomly selected raw
325 data for four anomalous days from each station, as shown in Fig. 9.
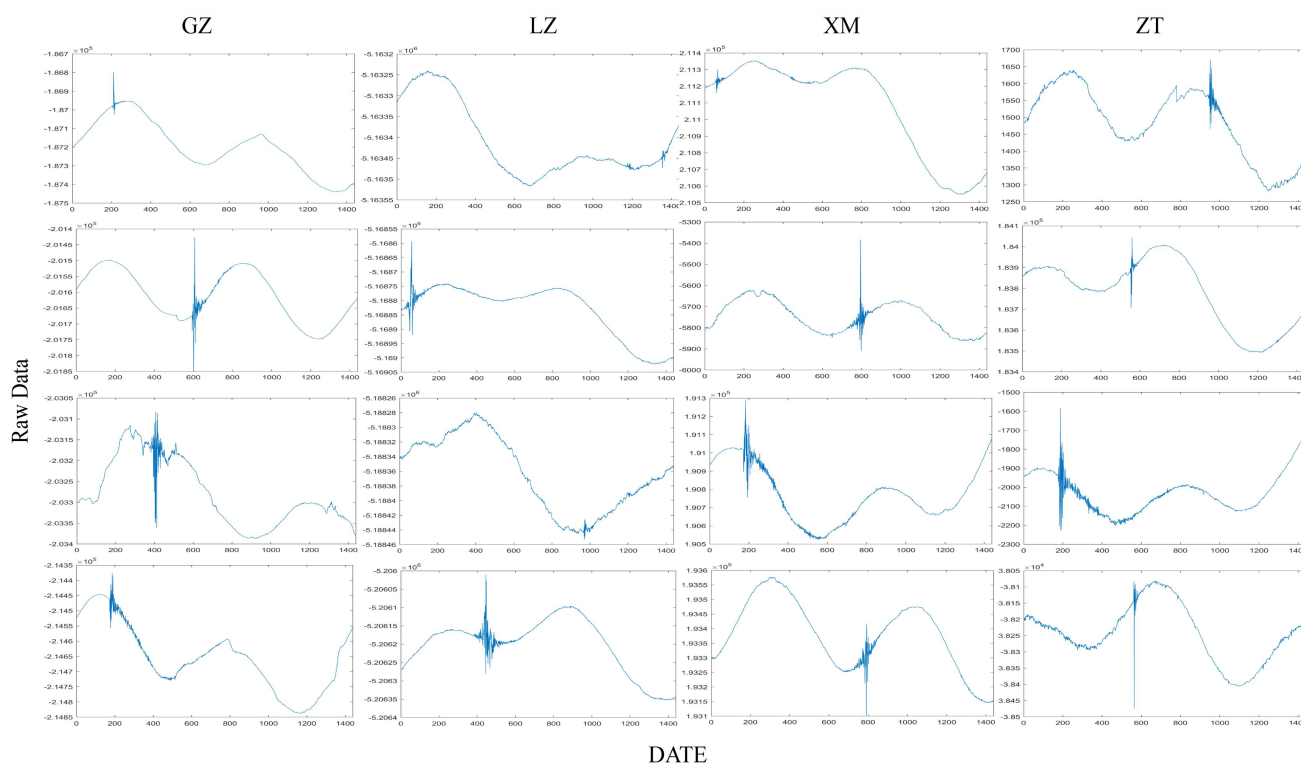
Figure 9: Plots of raw data from four randomly selected anomalous days at each station.

In Fig. 9, it is evident that the abnormal days we defined exhibit short-period, high-frequency oscillation signals in the original waveform, suggesting that these days are associated with crustal activity. The cumulative values of the anomalous
330 days over time are depicted in Fig. 10.
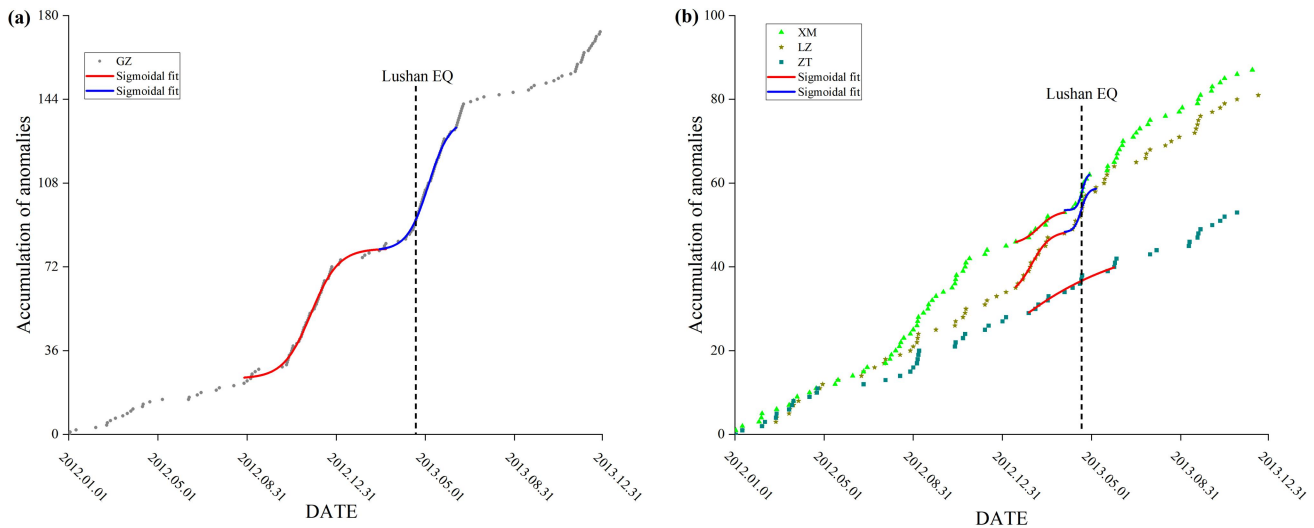
Figure 10: Accumulation results of anomalous days in borehole data from each station. The dashed line indicates the date of the earthquake, while the red and blue curves indicate the results of the S-shaped fitting before and after the earthquake, respectively. (a) Anomalous day accumulation results for Guza station; (b) Anomalous day accumulation results for Xiaomiao, Luzhou, and Zhaotong stations.

As depicted in Fig. 10a, the cumulative results of the anomalous days at Guza station exhibit a two-part concavity. One part displayed a rapid increase in the number of anomalous days from October 2012 to three months before the earthquake (January 2013), after which it leveled off. Our findings align with those of Chi et al., (2013) and Zhu et al., (2018), indicating that strain anomalies occurred during the 4-8 months preceding the earthquake, and the accumulation of anomalous days exhibited an accelerating trend. In the other segment, the number of anomalous days started to rise sharply from March 2013 to June after the earthquake, after which the increase in anomalous days gradually leveled off. Qiu et al. (An et al., 2013; Jiang et al., 2013; Yu et al., 2020; Qiu et al., 2013; Zhu et al., 2018) conducted research on short-term impending earthquake anomalies pre-ceding the Lushan earthquake and suggested that these anomalies occurred within a few days to one month before the earthquake. Our study yielded similar results, indicating anomalies in the one-month pre-earthquake period of the Lushan earthquake. Therefore, we posit that these anomalies might be related to the Lushan earthquake. The findings of Yu et al., (2021), who observed a brief increase in anomalies followed by a return to a steady state in the two-month post-earthquake period, align closely with the outcomes of our study.

In Fig. 10b, we analyzed the anomalous day accumulation at other stations within the graph wavenet network. Remarkably, the accumulation patterns of anomalous days at Xiaomiao and Luzhou closely mirrored those observed at Guza, featuring concave trends in two distinct phases. However, the fitting results for the Zhaotong station deviated from the observed pattern. Analyzing the aforementioned fitting results, we observed a similar trend between the Xiaomiao and Luzhou stations, resembling the patterns identified at the Guza station. The initial phase witnessed a sharp increase in January 2013 and plateaued until March 2013, indicating an accelerated accumulation of abnormal days in the four months leading up to the earthquake. In the second phase, spanning from 5 April 2013 to 28 April 2013, a surge was apparent 15

355   days prior to the earthquake, followed by a gradual decline 8 days post-earthquake. This pattern echoes the impending and post-earthquake anomalies observed at the Guza Station during the Lushan earthquake. A detailed analysis indicates that the Xiaomiao and Luzhou stations also detected anomalous signals during the gestation process of the Lushan earthquake, affirming that the anomalies at these three stations were not random but were indeed linked to the Lushan earthquake. Further scrutiny of the distances between the stations and the epicenter revealed a noteworthy pattern: Guza station, which

360   was the closest to the epicenter, record-ed the highest number of anomalous days; Xiaomiao and Luzhou stations, in proximity to the epicenter, registered fewer anomalous days than Guza station, whereas Zhaotong station, situated farthest from the epicenter, reported the fewest anomalous days. This lends credence to the belief that the anomalous signals received by a station are associated with the distance between the station and epicenter.

         Zhang et al., (2020) conducted an analysis of cross-fault deformation preceding the Lushan Ms7.0 earthquake. Their

365   findings revealed a considerable shift in the cross-fault deformation dynamics of the study area, transitioning from a state of "inheritance," conducive to stress accumulation, to "reverse inheritance" more than six months prior to the earthquake. This shift exhibits characteristics of coordinated and accelerated fault activities, aligning with the metastable and sub-unstable states observed in the structural mechanics tests. Notably, earthquakes with magnitudes exceeding 4 in the study area exhibited a robust structural correlation with the Lushan Ms7.0 earthquake, potentially indicating a partial release of energy

370   in the locked section of the fault. In summary, our analysis suggests that 4-8 months prior to the Lushan Ms7.0 earthquake, the southern section of the Longmenshan rupture exhibited characteristics of a sub-stabilized state. This state led to the formation of relatively weak segments on the fault, contributing to an increase in the number of anomalous days potentially associated with the pre-release of energy. Simultaneously, the relatively strong fault segments underwent strain accumulation. In the days immediately preceding the earthquake, these strong segments reached a destabilized state owing to the

375   accumulated strain, ultimately facilitating the occurrence of an earthquake (Ma and Guo, 2014).
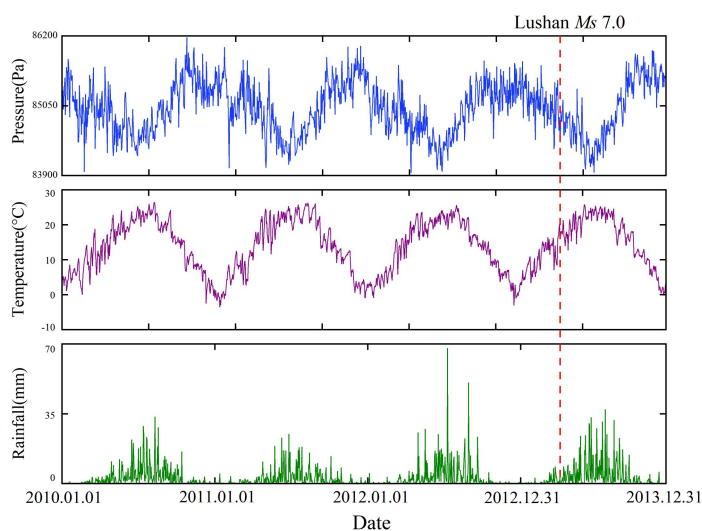
Figure 11: Regional daily mean variations in pressure, temperature, and rainfall in the Lushan area from 2010 to 2013.

...

Despite its advantages, such as high sensitivity and a wide frequency band during observation, the four-component borehole strainmeter remains susceptible to interference from surrounding sources. Figure 11 illustrates the impact of external factors by examining the regional daily mean data of pressure, temperature, and rainfall in the Lushan region (102° E, 27° N, 106° E, and 31° N), downloaded from 1 January 2010 to 31 December 2013, via NASA's Giovanni-4 platform (https://giovanni.gsfc.nasa.gov/giovanni). The analysis of these data revealed distinct annual trends in pressure, temperature, and rain-fall. Both pressure and temperature exhibited fluctuations within a certain range, dis-playing opposite trends, whereas rainfall underwent a consistent increase followed by a decrease each year, in accordance with seasonal changes. To mitigate the impact of external factors on borehole strain data, we conducted a differencing process on the daily regional averages for pressure, temperature, and rainfall in the Lushan area. The results are shown in Fig. 12.
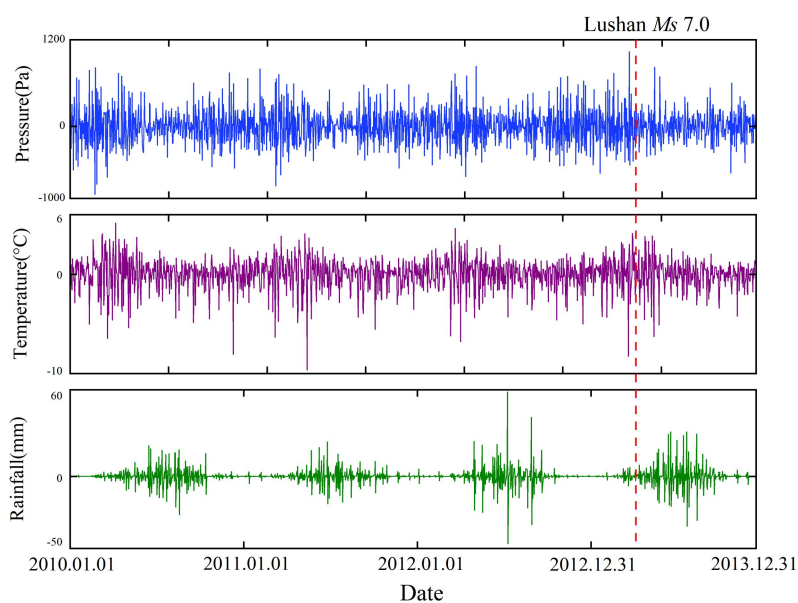
Figure 12: Differing results of regional daily mean pressure, temperature, and rainfall in the Lushan area from 2010 to 2013.

Figure 12 indicates that the regional daily mean differences in pressure, temperature, and rainfall in the Lushan area did not exhibit any anomalous changes. Therefore, we can exclude the influence of pressure, temperature, and rainfall on the anomalies observed in the pre-earthquake borehole data from Lushan.

6 Conclusion

In this study, we proposed a novel pre-earthquake anomaly extraction method based on a graph wavenet network structure that enables the integration of borehole strain data from multiple stations and makes predictions by learning both temporal and spatial correlations. The statistical analysis of pre-earthquake anomalies in borehole strain data from four stations, Guza, Xiaomiao, Luzhou, and Zhaotong, revealed two S-shaped upward trends in the pre-earthquake period for Guza, Xiaomiao,

and Luzhou. This indicates that these three stations experienced notable strain anomalies during the gestational period of the Lushan earthquake. A comparison of anomaly accumulation rates among different stations indicated that the anomaly rate at Guza station was substantially higher than that at Xiaomiao and Luzhou stations, suggesting a correlation with distance from the epicenter. Raw data analysis of randomly selected anomalous days from each station confirmed the correlation between the extracted anomalous days and the pre-earthquake anomalies. Additionally, we analyzed regional daily averages of meteorological factors, preliminarily excluding their influence on the anomaly accumulation results. Therefore, we conclude that the graph wavenet network effectively extracted pre-earthquake anomalies from borehole strain data, highlighting its potential as a robust approach for studying pre-earthquake anomalies across multiple stations.

Author Contributions. Conceptualization, Chenyang Li and Chengquan Chi; Data curation , Chenyang Li, Chengquan Chi and Yu Duan; Formal analysis, Chenyang Li, Chengquan Chi, Ying Han, and Zining Yu; Investigation, Chenyang Li; Methodology, Chengquan Chi; Resources, Chengquan Chi; Software, Chenyang Li and Dewang Zhang; Supervision, Chengquan Chi, Zining Yu and Ying Han; Validation, Chenyang Li, Chengquan Chi, and Ying Han; Writing – original draft, Chengquan Chi and Ying Han; Writing – review & editing, Chenyang Li and Chengquan Chi.

Competing interests. The authors declare that they have no conflict of interest.

Acknowledgments. The authors would like to thank Qiu Z. H., and Yang D. H. from the China Earthquake Administration for giving essential help in accessing the website and downloading the strain data. The authors are also grateful to the Giovanni for meteorological da-ta(https://giovanni.gsfc.nasa.gov/giovanni).

Financial support. This work was supported by the Hainan Provincial Natural Science Foundation of China under Grants 621QN242,622RC669, 621QN0888, 322RC659 and 320QN253, as well as by the Pro-gram of Hainan Association for Science and Technology Plans to Youth R & D Innovation under Grants: QCXM202006; This work is supported by the Fundamental Research Funds for the Central Universities under Grants 202213042 and Youth Fund of the National Natural Science Foundation of China, project number:42204005.

References

An, Z., Du, X., Tan, D., Fan, Y., Liu, J., and Cui, T.: Study on the Geo-Electric Field Variation of Sichuan Lushan MS7.0 and Wenchuan MS8.0 Earthquake, Chinese Journal of Geophysics, 56, 721-730, https://doi.org/10.1002/cjg2.20065, 2013.

Bilal, M. A., Ji, Y., Wang, Y., Akhter, M. P., and Yaqub, M.: Early Earthquake Detection Using Batch Normalization Graph Convolutional Neural Network (BNGCNN), Applied Sciences, 12, 10.3390/app12157548, 2022.

Campbell, L. R., Menegon, L., Fagereng, Å., and Pennacchioni, G.: Earthquake nucleation in the lower crust by local stress amplification, Nature Communications, 11, 10.1038/s41467-020-15150-x, 2020.

Chen, P., Yao, Y., Chen, J., Yao, W., and Zhu, X.: Study of the 2013 Lushan M7.0 earthquake coseismic ionospheric disturbances, Advances in Space Research, 54, 2194-2199, 10.1016/j.asr.2014.08.014, 2014.

Chi, C., Li, C., Han, Y., Yu, Z., Li, X., and Zhang, D.: Pre-earthquake anomaly extraction from borehole strain data based on machine learning, Scientific Reports, 13, 10.1038/s41598-023-47387-z, 2023.

435 Chi, C., Zhu, K., Yu, Z., Fan, M., Li, K., and Sun, H.: Detecting Earthquake-Related Borehole Strain Data Anomalies With Variational Mode Decomposition and Principal Component Analysis: A Case Study of the Wenchuan Earthquake, IEEE Access, 7, 157997-158006, 10.1109/access.2019.2950011, 2019.

Chi, S.: Strain Anomalies Before Wenchuan and Lushan Earthquakes Recorded by Component Borehole Strainmeter, Science & Technology Review, 31, 27-30, 10.3981/j.issn.1000-7857.2013.12.004, 2013.

440 Chi, S., Wu, H., and Luo, M.: Discussion on strain tidal factor separation and anisotropy——Analysis of first data of borehole component strain-meter of China's digital seismological observational networks, Progress in GeophysicsVL - 22, 1746-1753, 2007.

Chi, S., Liu, Q., Chi, Y., Deng, T., Liao, C., Yang, G., Zhang, G., and Chen, J.: Borehole strain anomalies before the 20 April 2013 Lushan Ms7.0 earthquake, Acta Seismologica Sinica, 35, 296-303, 10.3969/j.issn.0253-3782.2013.03.002, 2013.

445 Dobrovolsky, I. P., Zubkov, S. I., and Miachkin, V. I.: Estimation of the size of earthquake preparation zones, pure and applied geophysics, 117, 1025-1044, 10.1007/BF00876083, 1979.

Dragomiretskiy, K. and Zosso, D.: Variational Mode Decomposition, IEEE Transactions on Signal Processing, 62, 531-544, 10.1109/tsp.2013.2288675, 2014.

Fan, J., Meng, J., Ludescher, J., Chen, X., Ashkenazy, Y., Kurths, J., Havlin, S., and Schellnhuber, H. J.: Statistical physics
450 approaches to the complex Earth system, Physics Reports, 896, 1-84, 10.1016/j.physrep.2020.09.005, 2021.

Guo, K. and Zheng, Y.: Big Data-based Abnormal Analysis of Seismic Background Noise before Strong Earthquake The Case of the Lushan Ms7.0 Earthquake, EARTHQUAKE RESEARCH IN CHINA, 38, 503-512, 2022.

Hong, H., Xu, H., Song, F., Zhang, X., and Li, G.: Discussion on seismo-geological hazards induced by 2013 Lushan Ms7.0 earthquake and its seismogenic fault, Acta Seismologica Sinica, 35, 738-748, 10.3969/j.issn.0253-3782.2013.05.012, 2013.

455 Huang, Y., Yan, L., Cheng, Y., Qi, X., and Li, Z.: Coal Thickness Prediction Method Based on VMD and LSTM, Electronics, 11, 10.3390/electronics11020232, 2022.

Huang, Y., Shi, W., Zhu, K. a., Qiu, H., Lu, Y., Liu, G., and Zhang, G.: A pre-seismic anomaly detection approach based on graph attention isomorphism network, Measurement Science and Technology, 34, 10.1088/1361-6501/acefeb, 2023.

Jiang, W., Ma, Y., Liu, H., Deng, L., and Zhou, X.: Investigation of Lushan earthquake ionosphere VTEC anomalies based
460 on GPS data, Earthquake Science, 26, 259-265, 10.1007/s11589-013-0013-4, 2013.

Kim, G., Ku, B., Ahn, J.-K., and Ko, H.: Graph Convolution Networks for Seismic Events Classification Using Raw Waveform Data From Multiple Stations, IEEE Geoscience and Remote Sensing Letters, 19, 1-5, 10.1109/lgrs.2021.3127874, 2022.

Kipf, T. N. and Welling, M.: Semi-Supervised Classification with Graph Convolutional Networks, arXiv e-prints,
465 arXiv:1609.02907, 10.48550/arXiv.1609.02907, 2016.

Liu, C., Wang, G., Shi, Z., and Zhao, D.: Groundwater precursor anomalies of the 7.0 Sichuan Lushan earthquake, China Geoscience Joint Annual Conference 2014 - Topic 10: Fluid geoscience and the genesis of mega-mineralized zones and major natural disasters, 4,

Liu, Q., Shen, X., Zhang, J., and Li, M.: Exploring the abnormal fluctuations of atmospheric aerosols before the 2008
470 Wenchuan and 2013 Lushan earthquakes, Advances in Space Research, 63, 3768-3776, 10.1016/j.asr.2019.01.032, 2019.

Liu, Q., Zhang, J., Chi, S., and Yan, W.: Time-frequency characteristics of four-component borehole strain at Guzan station before and after 2013 Lushan Ms 7.0 earthquake, Acta Seismologica Sinica, 36, 770-779, 10.3969/j.issn.0253-3782.2014.05.002, 2014b.

Ma, J. and Guo, Y.: Accelerated synergism prior to fault instability: Evidence from laboratory experiments and an
475 earthquake case, Dizhen Dizhi, 36, 547-561, 10.3969/j.issn.0253-4967.2014.03.001, 2014.

Ma, W., Kong, X., Kang, C., Zhong, X., Wu, H., Zhan, X., and Joshi, M.: Research on the changes of the tidal force and the air temperature in the atmosphere of Lushan (China) Ms7.0 earthquake, Thermal Science, 19, 487-493, 10.2298/tsci150403148m, 2015.

Niepert, M., Ahmed, M., and Kutzkov, K.: Learning Convolutional Neural Networks for Graphs, arXiv e-prints,
480 arXiv:1605.05273, 10.48550/arXiv.1605.05273, 2016.

Oord, A. v. d., Dieleman, S., Zen, H., Simonyan, K., Vinyals, O., Graves, A., Kalchbrenner, N., Senior, A., and Kavukcuoglu, K.: WaveNet: A Generative Model for Raw Audio, arXiv e-prints, arXiv:1609.03499, 10.48550/arXiv.1609.03499, 2016.

485 Qiu, Z.: On monitoring precursors of major earthquakes with dense network of borehole strainmeters, Acta Seismologica Sinica, 36, 738-749, 10.3969/j.issn.0253-3782.2014.04.019, 2014.

Qiu, Z., Kan, B., and Tang, L.: Conversion and application of 4-component borehole strainmeter data, EARTHQUAKE, 29, 83-89, 2009.

Qiu, Z., Tang, L., Guo, Y., and Zhang, B.: Decade borehole strain observation at Guza and the precursory anomaly of the Wenchuan earthquake, Progress in GeophysicsVL - 35, 1299-1309, 10.6038/pg2020CC0237, 2020.

490 Qiu, Z., Yang, G., Tang, L., Guo, Y., and Zhang, B.: Abnormal strain changes observed by a borehole strainmeter at Guza Station before the Ms7.0 Lushan earthquake, Geodesy and Geodynamics, 4, 19-29, 10.3724/sp.J.1246.2013.03019, 2013.

Rathore, N., Rathore, P., Basak, A., Nistala, S. H., and Runkana, V.: Multi Scale Graph Wavenet for Wind Speed Forecasting, arXiv e-prints, arXiv:2109.15239, 10.48550/arXiv.2109.15239, 2021.

Scarselli, F., Gori, M., Tsoi, A. C., Hagenbuchner, M., and Monfardini, G.: The Graph Neural Network Model, IEEE 495 Transactions on Neural Networks, 20, 61-80, 10.1109/tnn.2008.2005605, 2009.

Su, K.: Analysis of Surface Strain and Shear Strain from Four Component Borehole Strain Observation Data, Earthquake Research in Shanxi, 1, 30-35,52, 2019.

Tang, L. and Jing, Y.: Analysis of Coseismic Strain Step Observed by 4-Component Borehole Strain Meters in Sichuan-Yunnan Region, Technology for Earthquake Disaster Prevention, 8, 370-376, 2013.

500 Wu, Z., Pan, S., Chen, F., Long, G., Zhang, C., and Yu, P. S.: A Comprehensive Survey on Graph Neural Networks, arXiv e-prints, arXiv:1901.00596, 10.48550/arXiv.1901.00596, 2019.

Yu, B., Yin, H., and Zhu, Z.: Spatio-Temporal Graph Convolutional Networks: A Deep Learning Framework for Traffic Forecasting, arXiv e-prints, arXiv:1709.04875, 10.48550/arXiv.1709.04875, 2017.

Yu, Z., Hattori, K., Zhu, K., Chi, C., Fan, M., and He, X.: Detecting Earthquake-Related Anomalies of a Borehole Strain 505 Network Based on Multi-Channel Singular Spectrum Analysis, Entropy, 22, 10.3390/e22101086, 2020.

Yu, Z., Zhu, K., Hattori, K., Chi, C., Fan, M., and He, X.: Borehole Strain Observations Based on a State-Space Model and ApNe Analysis Associated With the 2013 Lushan Earthquake, IEEE Access, 9, 12167-12179, 10.1109/access.2021.3051614, 2021.

Zhang, B.: PLATE BOUNDARY OBSERVATION (PBO) PROJECT OF USA, Journal of Geodesy and Geodynamics, 24, 510 105-108, 2004.

Zhang, J. and He, X.: Earthquake magnitude prediction using a VMD-BP neural network model, Natural Hazards, 117, 189-205, 10.1007/s11069-023-05856-8, 2023.

Zhang, X., Liu, X., Qin, S., and Jia, P.: Precursory Characteristics of Meta-Instability of Cross-Fault Deformation Before the Lushan Ms 7.0 Earthquake, Geomatics and Information Science of Wuhan University, 45, 1669-1677, 515 10.13203/j.whugis20190467, 2020.

Zhang, Y., Huang, H., and Cheng, X.: Thermal anomaly detection for 2013 Lushan earthquake, 2016 IEEE International Geoscience and Remote Sensing Symposium (IGARSS), 10-15 July 2016, 2849-2852, 10.1109/IGARSS.2016.7729736,

Zheng, X. and Zhang, C.: U.S. ' Earth Lens Program ', Recent Developments in World Seismology, 22-41, 2004.

Zhou, J., Cui, G., Hu, S., Zhang, Z., Yang, C., Liu, Z., Wang, L., Li, C., and Sun, M.: Graph neural networks: A review of 520 methods and applications, AI Open, 1, 57-81, 10.1016/j.aiopen.2021.01.001, 2020.

Zhu, K., Chi, C., Yu, Z., Zhang, W., Fan, M., Li, K., and Zhang, Q.: Extracting borehole strain precursors associated with the Lushan earthquake through principal component analysis, Annals of Geophysics, 61, 10.4401/ag-7633, 2018.

Zhu, Y., Wen, X., Sun, H., Guo, S., and Zhao, Y.: Gravity changes before the Lushan, Sichuan, Ms=7.0 Earthquake of 2013, Chinese Journal of Geophysics- Chinese Edition, 56, 1887-1894, 10.6038/cjg20130611, 2013.

525